Journal of Applied Physics

TUTORIAL | AUGUST 24 2026

Four-phonon thermal conductivity: Numerical sensitivities, convergence, and machine-learning acceleration

Ankit Jain ; Rajan Kumar ; Jyotishraj Thoudam ; Nidheesh Virakante

Check for updates

J. Appl. Phys. 140, 081101 (2026)
https://doi.org/10.1063/5.0348402

View Online Export Citation

Articles You May Be Interested In

Revisiting thermal transport in CuInTe 2 : Role of temperature-dependent anharmonicity and higher-order phonon–phonon interactions

Appl. Phys. Lett. (July 2024)

First-principles prediction of thermal conductivity of bulk hexagonal boron nitride

Appl. Phys. Lett. (April 2024)

Lattice thermal conductivity of 16 elemental metals from molecular dynamics simulations with a unified neuroevolution potential

J. Appl. Phys. (June 2025)

23 October 2026 05:10:15

Nanotechnology & Materials Science
Optics & Photonics
Impedance Analysis
Scanning Probe Microscopy
Sensors
Failure Analysis & Semiconductors

Unlock the Full Spectrum.
From DC to 8.5 GHz.



Zurich Instruments

Find out more

AIP Publishing

Journal of Applied Physics TUTORIAL pubs.aip.org/aip/jap

Four-phonon thermal conductivity: Numerical sensitivities, convergence, and machine-learning acceleration

Cite as: J. Appl. Phys. **140**, 081101 (2026); doi: 10.1063/5.0348402
Submitted: 16 June 2026 · Accepted: 4 August 2026 ·
Published Online: 24 August 2026

View Online Export Citation CrossMark

Ankit Jain,[a] Rajan Kumar, Jyotishraj Thoudam, and Nidheesh Virakante

AFFILIATIONS

Department of Mechanical Engineering, IIT Bombay, Mumbai 400076, India

[a]**Author to whom correspondence should be addressed:** a_jain@iitb.ac.in

ABSTRACT

While the prediction of lattice thermal conductivity has traditionally relied on three-phonon interaction frameworks, accurately modeling highly anharmonic materials or extreme temperature regimes increasingly demands the inclusion of higher-order effects. This tutorial presents a comprehensive computational framework for predicting four-phonon scattering processes and the associated phonon thermal conductivity. The physical conditions that necessitate fourth-order interactions are first outlined, followed by a detailed analysis of quartic interatomic force constant (IFC) extraction, four-phonon scattering calculations, and machine-learning acceleration modules. Utilizing Lennard-Jones argon and Stillinger–Weber silicon as model systems, a systematic sensitivity analysis is performed to isolate the numerical artifacts and error propagation inherent to finite-difference routines vs Taylor-series regression-fitting methods for quartic IFC extraction. The role of primary density functional theory parameters, specifically plane wave energy cutoffs, electronic ***k***-point grids, minimization algorithms, and parallelization schemes, on the fidelity of computed atomic forces is established using cubic boron arsenide as a representative test system. Crucially, the convergence behavior of four-phonon-driven thermal conductivity across various numerical parameters is shown to be highly material-dependent. Finally, it is demonstrated that the severe computational bottlenecks traditionally associated with establishing parameter convergence can be effectively mitigated by integrating machine-learning-accelerated approaches, offering a robust paradigm for next-generation, high-fidelity transport simulations.

Published under an exclusive license by AIP Publishing. https://doi.org/10.1063/5.0348402

23 October 2026 05:10:15

I. INTRODUCTION

The fundamental understanding of thermal transport in crystalline solids is a cornerstone for advancing technologies ranging from thermoelectric energy harvesting to thermal management in high-power electronics and nuclear energy systems.[1] Historically, the discovery of materials with tailored thermal conductivity relied on empirical heuristics and iterative experimental characterization.[2] However, recent advances in first-principles computational frameworks have catalyzed a paradigm shift, enabling the parameter-free prediction of κ via the Peierls–Boltzmann Transport Equation (BTE) coupled with density functional theory (DFT).[3–7] This predictive methodology has achieved remarkable success in describing and enabling the extraction of physical insights of thermal transport in semiconductors and low-dimensional systems, including silicon, gallium nitride, and carbon nanotubes.[8–12]

In non-metallic crystals, the main thermal energy carriers are phonons—the quantized collective excitations of the crystal lattice.[13–16] For decades, lowest-order three-phonon scattering has stood as the theoretical gold standard for modeling phonon-mediated thermal conductivity.[6,7,17] However, this truncation to the lowest order has been found insufficient to describe the anomalous transport behavior in high-thermal-conductivity materials such as boron arsenide (BAs).[18–21] Emerging evidence indicates that the three-phonon approximation also breaks down under other physical conditions because it fails to account for full higher-order lattice anharmonicity.[20,22–24] Resolving these discrepancies requires an expanded description of transport that incorporates higher-order corrections, including four-phonon scattering,[25] temperature-dependent phonon-frequency renormalization,[26] and multi-channel transport dynamics.[27] This tutorial delivers a rigorous treatment of four-phonon scattering theory, providing a

Published under an exclusive license by AIP Publishing

comprehensive framework for modeling material systems where lower-order approximations fail to capture the underlying physics.

The phonon thermal conductivity (κ) is obtainable by summing up contributions from particle-channels (κ^p, also referred to as the population-channel) and wave-like coherent-channels (κ^c) as[27]

$$\kappa = \kappa^p + \kappa^c. \tag{1}$$

The contribution from the particle-channel can be obtained using the BTE[7,17] and that from the coherent-channel can be evaluated from the Wigner formalism.[27] The particle-channel contribution in the α direction, for an applied heat flux in the β-direction, is given by[16,28,29]

$$\kappa^p_{\alpha\beta} = \sum_{\boldsymbol{q}} \sum_{\nu} c_{\boldsymbol{q}\nu} v_{\boldsymbol{q}\nu,\alpha} v_{\boldsymbol{q}\nu,\beta} \tau_{\boldsymbol{q}\nu,\alpha}, \tag{2}$$

where c, v, and τ are the phonon volumetric specific heat, group velocity, and scattering time, respectively, and the summation is over all the phonon modes with wave vector $\boldsymbol{q}$ and polarization ν. The coherent-channel contribution is given by[27]

$$\kappa^c_{\alpha\beta} = \frac{\hbar^2}{k_B T^2} \frac{1}{VN} \sum_{\boldsymbol{q}} \sum_{(\nu \neq \nu_1)} \frac{\omega_{\boldsymbol{q}\nu} + \omega_{\boldsymbol{q}\nu_1}}{2} V^{\alpha}_{\boldsymbol{q},\nu\nu_1} V^{\beta}_{\boldsymbol{q},\nu_1\nu} \times \frac{\omega_{\boldsymbol{q}\nu} n_{\boldsymbol{q}\nu}(n_{\boldsymbol{q}\nu}+1) + \omega_{\boldsymbol{q}\nu_1} n_{\boldsymbol{q}\nu_1}(n_{\boldsymbol{q}\nu_1}+1)}{4(\omega_{\boldsymbol{q}\nu} - \omega_{\boldsymbol{q}\nu_1})^2 + (\Gamma_{\boldsymbol{q}\nu} + \Gamma_{\boldsymbol{q}\nu_1})^2} (\Gamma_{\boldsymbol{q}\nu} + \Gamma_{\boldsymbol{q}\nu_1}), \tag{3}$$

where $\hbar$ is the reduced Planck constant, k_B is the Boltzmann constant, T is the temperature, V is the unit-cell volume, N is the number of $\boldsymbol{q}$-points, ω is the phonon frequency, n is the Bose–Einstein distribution ($n_{\boldsymbol{q}\nu} = \frac{1}{e^x - 1}$ with $x = \frac{\hbar\omega_{\boldsymbol{q}\nu}}{k_B T}$), Γ is the phonon linewidth ($\Gamma_{\boldsymbol{q}\nu} = 1/\tau_{\boldsymbol{q}\nu}$), and $V^{\alpha}_{\boldsymbol{q},\nu\nu_1}$ is the α-component of the velocity operator.[27] The readers are referred to our previous tutorial[7] for further details on the various quantities involved in Eq. (2) and the evaluation of thermal conductivity using three-phonon scattering with Eq. (2).

The evaluation of phonon thermal conductivity via Eqs. (2) and (3) requires phonon scattering rates. At the lowest level of theory, for intrinsic scattering, these scattering rates are obtained by considering three-phonon interactions [under the relaxation time approximation (RTA)] as

$$\frac{1}{\tau^{o,3ph}_{\boldsymbol{q}\nu}} = \sum_{\boldsymbol{q}_1\nu_1} \sum_{\boldsymbol{q}_2\nu_2} \left\{ \left\{ \left(n_{\boldsymbol{q}_1\nu_1} - n_{\boldsymbol{q}_2\nu_2}\right) W^{+} \right\} + \frac{1}{2} \left\{ \left(n_{\boldsymbol{q}_1\nu_1} + n_{\boldsymbol{q}_2\nu_2} + 1\right) W^{-} \right\} \right\}, \tag{4}$$

where $W^{\pm}$ represents the scattering probability matrix given by

$$W^{\pm} = \frac{2\pi}{\hbar^2} \left| \Psi^{\nu\nu_1\nu_2}_{\boldsymbol{q}(\pm\boldsymbol{q}_1)(-\boldsymbol{q}_2)} \right|^2 \delta(\omega_{\boldsymbol{q}\nu} \pm \omega_{\boldsymbol{q}_1\nu_1} - \omega_{\boldsymbol{q}_2\nu_2}), \tag{5}$$

with $\Psi^{\nu\nu_1\nu_2}_{\boldsymbol{q}\boldsymbol{q}_1\boldsymbol{q}_2}$ representing the Fourier transform of real-space cubic interatomic force constants (IFCs),

$$\Psi^{\nu\nu_1\nu_2}_{\boldsymbol{q}\boldsymbol{q}_1\boldsymbol{q}_2} = \Psi^{\nu\nu'\nu''}_{\boldsymbol{q}\boldsymbol{q}'\boldsymbol{q}''} = N \left(\frac{\hbar}{2N}\right)^{\frac{3}{2}} \sum_{b} \sum_{b'l'} \sum_{b''l''} \sum_{\alpha\beta\gamma} \Psi^{\alpha\beta\gamma}_{bl;b'l';b''l''} \times \frac{\tilde{e}^{\alpha}_{b,\boldsymbol{q}\nu} \tilde{e}^{\beta}_{b',\boldsymbol{q}'\nu'} \tilde{e}^{\gamma}_{b'',\boldsymbol{q}''\nu''}}{\sqrt{m_b \omega_{\boldsymbol{q}\nu} m_{b'} \omega_{\boldsymbol{q}'\nu'} m_{b''} \omega_{\boldsymbol{q}''\nu''}}} e^{\left[i\left(\boldsymbol{q}'\cdot\boldsymbol{r}_{0l'} + \boldsymbol{q}''\cdot\boldsymbol{r}_{0l''}\right)\right]}, \tag{6}$$

and $\delta()$ represents the Dirac-delta function ensuring energy conservation. Here, m_b is the mass of atom b in the unit cell, $\boldsymbol{r}_{bl}$ is the position vector of atom b in the l unit cell, $\tilde{e}^{\alpha}_{b,\boldsymbol{q}\nu}$ is the α-direction component of the normalized eigenvector $\tilde{\boldsymbol{e}}_{\boldsymbol{q}\nu}$, and α, β, γ represent the Cartesian directions. The summations in Eq. (6) are performed over phonon wavevectors that satisfy the condition for crystal momentum conservation, $\boldsymbol{q} + \boldsymbol{q}_1 + \boldsymbol{q}_2 = \boldsymbol{G}$, where $\boldsymbol{G}$ represents a reciprocal lattice vector.[13]

To go beyond RTA, the linearized BTE can be solved iteratively.[30] Furthermore, in the presence of additional scattering mechanisms, such as boundary, isotope, or defect scattering, the total scattering rates can be determined by combining the individual contributions according to the Matthiessen rule.[28,31,32]

While the lattice thermal conductivity derived from Eq. (2), accounting solely for three-phonon interactions, effectively captures the transport physics in traditional semiconductors such as Si, Ge, and GaAs,[9] this approximation reaches its limit in certain high-symmetry or strongly anharmonic systems.[24,29,33] This is particularly the case for materials characterized by extreme thermal conductivities or significant acoustic-optical gaps.[18] Recent studies indicate that omitting higher-order four-phonon processes leads to a substantial overestimation of phonon thermal conductivity, as four-phonon scattering provides a critical mechanism for phonon relaxation in regimes where the three-phonon phase space is intrinsically restricted.[20,22,34] In such scenarios, the four-phonon scattering rates must be incorporated in addition to the three-phonon rates defined in Eq. (4),

$$\frac{1}{\tau^{o,4ph}_{\boldsymbol{q}\nu}} = \sum_{\boldsymbol{q}_1\nu_1} \sum_{\boldsymbol{q}_2\nu_2} \sum_{\boldsymbol{q}_3\nu_3} \left\{ \frac{1}{6} \left\{ \frac{n_{\boldsymbol{q}_1\nu_1} n_{\boldsymbol{q}_2\nu_2} n_{\boldsymbol{q}_3\nu_3}}{n_{\boldsymbol{q}\nu_1}} W^{--} \right\} + \frac{1}{2} \left\{ \frac{(n_{\boldsymbol{q}_1\nu_1}+1) n_{\boldsymbol{q}_2\nu_2} n_{\boldsymbol{q}_3\nu_3}}{n_{\boldsymbol{q}\nu_1}} W^{+-} \right\} + \frac{1}{2} \left\{ \frac{(n_{\boldsymbol{q}_1\nu_1}+1)(n_{\boldsymbol{q}_2\nu_2}+1) n_{\boldsymbol{q}_3\nu_3}}{n_{\boldsymbol{q}\nu_1}} W^{++} \right\} \right\}, \tag{7}$$

where $W^{\pm\pm}$ are given by

$$W^{\pm\pm} = \frac{2\pi}{\hbar^2} \left| \Xi^{\nu\nu_1\nu_2\nu_3}_{\boldsymbol{q}(\pm\boldsymbol{q}_1)(\pm\boldsymbol{q}_2)(-\boldsymbol{q}_3)} \right|^2 \times \delta(\omega_{\boldsymbol{q}\nu} \pm \omega_{\boldsymbol{q}_1\nu_1} \pm \omega_{\boldsymbol{q}_2\nu_2} - \omega_{\boldsymbol{q}_3\nu_3}), \tag{8}$$

with $\Xi^{\nu\nu_1\nu_2\nu_3}_{\boldsymbol{q}(\pm\boldsymbol{q}_1)(\pm\boldsymbol{q}_2)(-\boldsymbol{q}_3)}$ representing the Fourier transformation of

23 October 2026 05:10:15

Published under an exclusive license by AIP Publishing

real-space quartic IFCs,

$$\Xi^{\nu\nu_1\nu_2\nu_3}_{\mathbf{q}\mathbf{q}_1\mathbf{q}_2\mathbf{q}_3} = \Xi^{\nu\nu'\nu''\nu'''}_{\mathbf{q}\mathbf{q}'\mathbf{q}''\mathbf{q}'''} = N\left(\frac{\hbar}{2N}\right)^2 \sum_{b}\sum_{b'l'}\sum_{b''l''}\sum_{b'''l'''}\sum_{\alpha\beta\gamma\delta} \Xi^{\alpha\beta\gamma}_{bl;b'l';b''l'';b'''l'''} \times \frac{\tilde{e}^{\alpha}_{b,\mathbf{q}\nu}\tilde{e}^{\beta}_{b',\mathbf{q}'\nu'}\tilde{e}^{\gamma}_{b'',\mathbf{q}''\nu''}\tilde{e}^{\delta}_{b''',\mathbf{q}'''\nu'''}}{\sqrt{m_b\omega_{\mathbf{q}\nu}m_{b'}\omega_{\mathbf{q}'\nu'}m_{b''}\omega_{\mathbf{q}''\nu''}m_{b'''}\omega_{\mathbf{q}'''\nu'''}}} \times e^{\left[i\left(\mathbf{q}'\cdot\mathbf{r}_{0l'}+\mathbf{q}''\cdot\mathbf{r}_{0l''}+\mathbf{q}'''\cdot\mathbf{r}_{0l'''}\right)\right]}. \quad (9)$$

$\delta()$ in Eq. (8) ensures that energy conservation and the summations in Eq. (9) are performed over phonon wavevectors that satisfy the condition for crystal momentum conservation, $\boldsymbol{q} + \boldsymbol{q}_1 + \boldsymbol{q}_2 + \boldsymbol{q}_3 = \boldsymbol{G}$.

Although the theoretical foundations of four-phonon scattering have existed for decades, their integration into robust computational frameworks is a recent development.[16,24–26,28,29] This tutorial focuses specifically on the numerical implementation and workflow of four-phonon scattering as formulated in Eqs. (7)–(9). For exhaustive theoretical derivations and a deeper exploration of the underlying scattering physics, readers are directed to Refs. 16 and 25. Notably, in materials characterized by ultralow thermal conductivity, additional corrections, including phonon frequency renormalization,[26] temperature-dependent potential-energy surfaces,[35] and multi-channel transport,[27] may also be required for a correct description of thermal transport.[17] However, a detailed treatment of these phenomena lies beyond the scope of this tutorial.

The remainder of this tutorial is structured as follows: Sec. II establishes the physical motivation and material-specific criteria that necessitate the inclusion of higher-order four-phonon scattering in thermal transport models. Next, Sec. III delineates the technical details of the computational pipeline, accompanied by an in-depth analysis of the inherent numerical complexities and scaling challenges unique to quartic processes. To translate these methodologies into practice, Sec. IV presents a comprehensive case study on BAs. This section provides a practical demonstration of workflow execution and systematic parameter convergence in regimes where higher-order anharmonic interactions are dominant. Section V compiles the openly available open-source computational packages to execute these advanced calculations. Finally, Secs. VI and VII present the future outlook and conclusions for this tutorial.

II. NEED FOR FOUR-PHONON SCATTERING

The necessity of incorporating higher-order four-phonon scattering into thermal transport models is motivated in Figs. 1(a) and 1(b). These figures illustrate the divergence between experimentally measured lattice thermal conductivity and the corresponding values computed solely within the conventional three-phonon approximation for silicon [Fig. 1(a)] and $CuInTe_2$ [Fig. 1(b)]. In the case of silicon, the lowest-order theory predicts a T^{-1} decay, whereas experimental data reveal a more pronounced $T^{-1.3}$ dependence[20] at elevated temperatures. Similarly, for $CuInTe_2$, the predicted decay of $T^{-1.02}$ from conventional

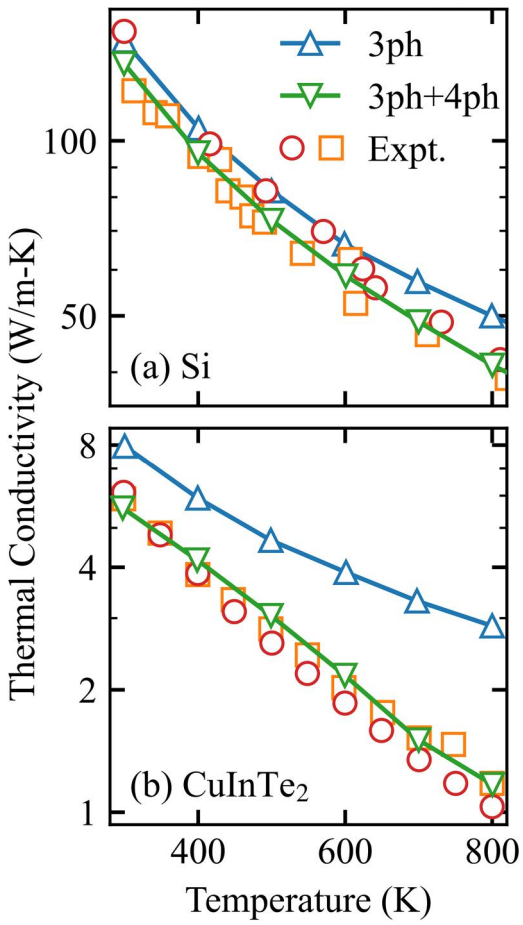


FIG. 1. Temperature-dependent lattice thermal conductivity of (a) Si and (b) $CuInTe_2$. For the relatively harmonic Si, three-phonon scattering is sufficient near room temperature, whereas four-phonon scattering is required at elevated temperatures. In contrast, for the strongly anharmonic $CuInTe_2$, the explicit inclusion of four-phonon scattering is necessary across the entire temperature range, including at room temperature. Computational results for Si are reproduced from Ref. 20, with corresponding experimental data from Refs. 38 and 39. For $CuInTe_2$, computational results are obtained from Ref. 36, and experimental data are from Refs. 40 and 41.

three-phonon theory fails to capture the experimentally observed $T^{-1.6}$–$T^{-1.8}$ scaling.[36] Notably, in both cases, the computationally obtained thermal conductivity falls in excellent agreement with experimental values, with the inclusion of four-phonon scattering.[37]

Other than at high temperature, the four-phonon scattering processes are non-negligible under the below discussed scenarios.

A. Suppressed three-phonon scattering phase space

In materials containing constituent elements with a large atomic mass mismatch, the contribution of three-phonon processes can be significantly constrained by the selection rules governing energy and momentum conservation, a phenomenon

23 October 2026 05:10:15

Published under an exclusive license by AIP Publishing

termed scattering phase-space restriction. Specifically, a large difference in atomic masses of participating species induces a wide frequency gap between the acoustic and optical phonon branches, which makes the available channels for three-phonon decay become severely limited due to difficulty in satisfying the energy conservation selection rule. When these lowest-order scattering pathways are limited, the thermal resistance becomes anomalously sensitive to higher-order interactions. In such regimes, four-phonon processes emerge as a dominant dissipative mechanism because they possess a significantly more expansive scattering phase space that bypasses the phase-space bottlenecks of the three-phonon framework. Consequently, the explicit inclusion of these quartic interactions is necessary for accurately predicting the thermal transport in materials such as boron arsenide[20,21] and θ-tantalum nitride.[42,43]

B. Symmetry suppressed three-phonon scattering

A related situation arises in two-dimensional (2D) planar materials, most notably graphene[44] and hexagonal monolayer boron nitride (h-BN).[45] In these systems, the reflection symmetry with respect to the horizontal midplane (the $z \rightarrow -z$ symmetry) imposes a rigorous selection rule on phonon scattering. This symmetry dictates that an anharmonic scattering process involving an odd number of "out-of-plane" flexural phonons (ZA) is strictly forbidden. Specifically, the three-phonon process involving three ZA phonons ($ZA + ZA \rightarrow ZA$) is nullified by this symmetry. Because flexural phonons have a high density of states at low frequencies and contribute significantly to heat capacity, the suppression of this primary scattering channel led to a very large/divergent thermal conductivity when only three-phonon interactions are considered. Four-phonon scattering processes also obey reflection symmetry. However, they introduce additional symmetry-allowed scattering channels, while processes involving an odd number of ZA phonons remain forbidden. Interaction channels such as $ZA + ZA \rightarrow ZA + LA$ are also forbidden while $ZA + ZA \rightarrow ZA + ZA$ are symmetry-allowed and provide the necessary restorative mechanism for thermal equilibrium. Recent first-principles studies have demonstrated that at room temperature, these quartic interactions can reduce the predicted thermal conductivity of graphene by as much as 40%–60% compared to three-phonon only values.[46] Thus, in the 2D planar limit, four-phonon scattering is not a mere correction but a fundamental requirement for capturing the finite thermal resistance of the lattice.

C. Strongly anharmonic materials

While symmetry-imposed restrictions drive higher-order effects in high-κ materials, a different physical mechanism dominates in intrinsically low-thermal-conductivity systems such as Tl_3VSe_4[29] and lead chalcogenides.[24] These materials are characterized by strong lattice anharmonicity, often stemming from the presence of lone-pair electrons or proximity to a structural phase transition. In such systems, the potential-energy surface deviates significantly from the parabolic ideal. The large-amplitude vibrations of the constituent atoms explore the quartic (and higher) regions of the interatomic potential, rendering the lowest-order three-phonon scattering rates insufficient to describe the total phonon linewidth. Furthermore, these materials often exhibit significant phonon renormalization, where the phonon frequencies themselves shift significantly with temperature due to quartic interactions.[29] In Tl_3VSe_4, neglecting these effects results in an unphysical prediction of thermal transport, as the four-phonon scattering rates can be comparable in magnitude to three-phonon rates across a wide temperature range.[29,33]

D. High-temperature

As the temperature approaches or exceeds the Debye temperature of a material, the phonon population approaches the classical limit of the Bose–Einstein distribution, where the mode occupancy number simplifies to $n_{\mathbf{q}\nu} \approx k_B T/\hbar\omega_{\mathbf{q}\nu}$.[14] This linear population growth directly dictates the scaling behavior of the underlying anharmonic scattering rates. Specifically, while the standard three-phonon scattering rate scales linearly with temperature (T^1), the four-phonon scattering rate scales quadratically (T^2). This T^2 dependence arises mathematically from the involvement of an additional phonon mode within the scattering matrix element relative to the third-order process. Mechanistically, these elevated mode populations manifest as larger atomic vibrational amplitudes, enabling the system to probe deeper quartic regions of the interatomic potential-energy surface. Consequently, even in material systems where three-phonon scattering remains dominant under ambient conditions, four-phonon processes inevitably become more significant at elevated temperatures.

While accounting for four-phonon processes is essential under the extreme conditions or strongly anharmonic regimes described above, three-phonon scattering theory remains remarkably robust for modeling the thermal transport properties of many baseline material systems across broad temperature ranges.[5,7,9,11,47] For these conventional systems, the explicit inclusion of fourth-order scattering events often yields only marginal improvements in predictive accuracy while introducing a steep, often prohibitive, computational overhead. To contextualize these trade-offs, Sec. III outlines the implementation details for evaluating lattice thermal conductivity driven by both three- and four-phonon scattering mechanisms, with a particular emphasis on the distinct computational bottlenecks imposed by higher-order phonon interactions.

III. IMPLEMENTATION DETAILS

The evaluation of lattice thermal conductivity incorporating higher-order four-phonon scattering processes follows a hierarchical workflow (see Fig. 2), beginning with the baseline determination of harmonic and lowest-order anharmonic properties. To achieve an *ab initio*, parameter-free description of the underlying potential energy surface, the IFCs required to evaluate these properties are typically extracted from first-principles DFT calculations. These IFCs serve as the fundamental inputs for computing phonon scattering rates and subsequently solving the phonon BTE to determine the ultimate lattice thermal conductivity.

23 October 2026 05:10:15

Published under an exclusive license by AIP Publishing

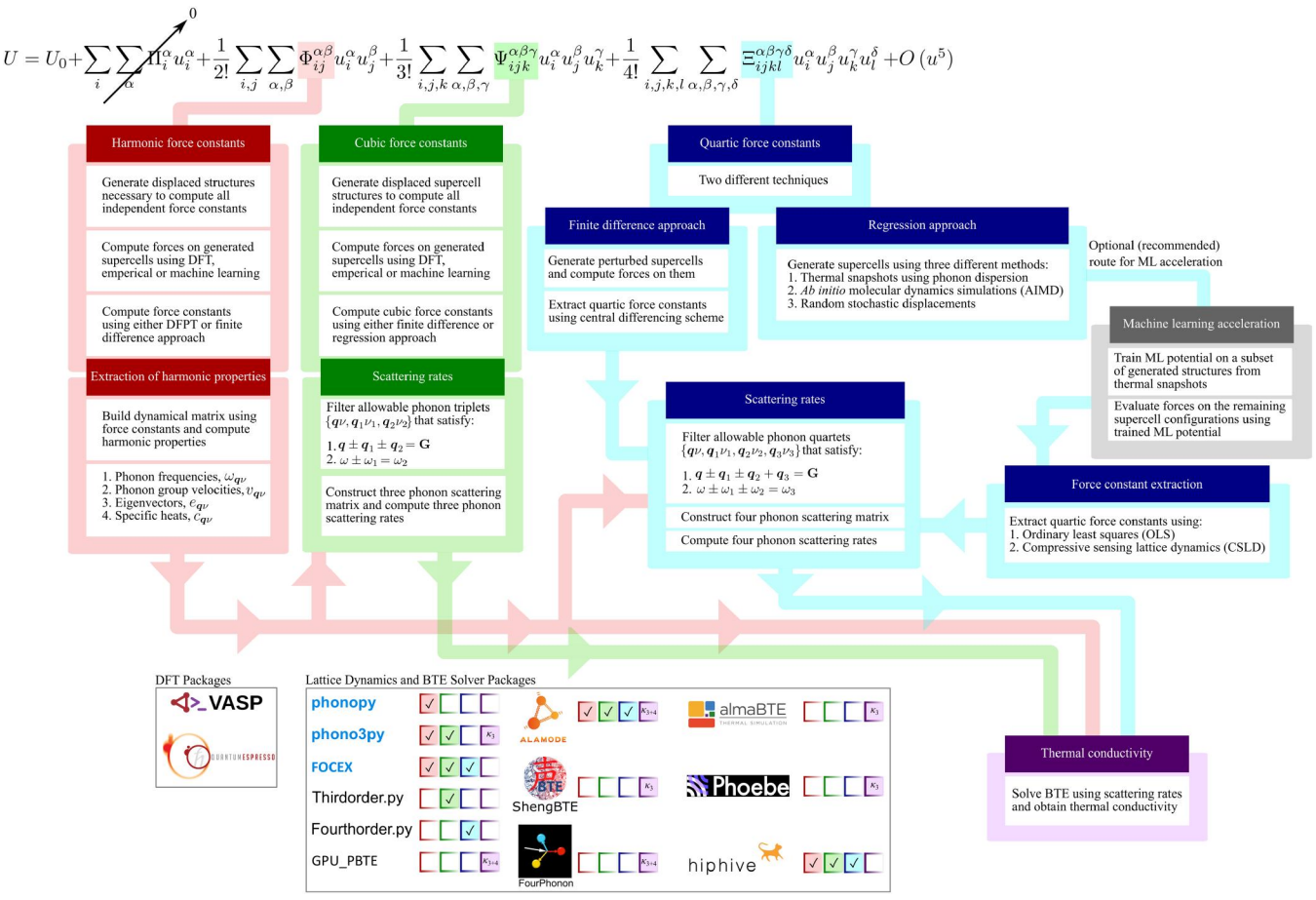


FIG. 2. The computational workflow for evaluating four-phonon-driven lattice thermal conductivity within the framework of the Boltzmann transport equation. The extraction pipelines and downstream calculations for harmonic, cubic, and quartic properties are color-coded in red, green, and blue, respectively. Widely utilized computational packages are compiled in the lower panel alongside their supported functionalities.

A. Step-1: Harmonic properties

The process starts with the evaluation of harmonic properties of the system, namely, phonon frequencies ($\omega_{q\nu}$) and eigenvectors ($e_{q\nu}$), which are determined by second-order (harmonic) IFCs. These harmonic quantities are routinely computed using either density functional perturbation theory or the finite-displacement method. In the finite-displacement approach, DFT is employed to calculate the restoring forces generated by small, systematic atomic displacements within a supercell framework; these forces are subsequently utilized to construct the dynamical matrix. Diagonalization of this dynamical matrix yields the complete phonon dispersion relations across the Brillouin zone, which concurrently provide the mode-resolved group velocities ($v_{q\nu}$) and modal heat capacities ($c_{q\nu}$) required for the subsequent transport formulations. Open-source software packages such as phonopy,[48] interfaced with popular DFT engines like VASP[49] or Quantum Espresso,[50] serve as the standard computational tools for extracting these essential harmonic quantities.

B. Step-2: Three-phonon-mediated thermal conductivity

Building upon these harmonic properties, the leading-order anharmonicity of the lattice is captured through the calculation of third-order IFCs. The extraction of these third-order IFCs is typically achieved either via a corresponding finite-displacement approach, which involves the simultaneous displacement of atom pairs to map out triplet interactions, or via a regression approach that employs force-displacement Taylor-series data-fitting optimized through least squares or least-absolute deviation minimization. These cubic IFCs govern the three-phonon scattering processes that constitute the primary source of intrinsic thermal resistance in most solid-state systems. Specialized toolkits such as

23 October 2026 05:10:15

Published under an exclusive license by AIP Publishing

thirdorder.py,[51] hiPhive,[52] and phono3py[48] are widely utilized to extract these cubic IFCs, while packages like phono3py and ShengBTE[51] serve as the standard tools for evaluating bulk phonon transport properties within this three-phonon scattering framework. For a comprehensive benchmarking of these tools, we direct readers to the recent "Phonon Olympics" study by McGaughey *et al.*,[53] which offers an independent and collaborative performance assessment of various software packages for three-phonon-limited lattice thermal conductivity.

Only after establishing these second- and third-order foundations can the framework be extended to include the quartic interactions necessary for four-phonon scattering. To extend the methodology, the framework must account for the next-highest-order term in the potential-energy expansion, i.e., quartic IFCs.

C. Step-3: Quartic IFCs

Beyond the third order, capturing higher-order lattice anharmonicity necessitates the explicit calculation of quartic IFCs. These constants characterize the fourth-order term in the Taylor expansion of the crystal potential energy (U) with respect to atomic displacements u_i^α of atom i along the α-direction from its equilibrium position,

$$U = U_0 + \sum_i \sum_\alpha \Pi_i^\alpha u_i^\alpha + \frac{1}{2!}\sum_{i,j}\sum_{\alpha,\beta} \Phi_{ij}^{\alpha\beta} u_i^\alpha u_j^\beta + \frac{1}{3!}\sum_{i,j,k}\sum_{\alpha,\beta,\gamma} \Psi_{ijk}^{\alpha\beta\gamma} u_i^\alpha u_j^\beta u_k^\gamma + \frac{1}{4!}\sum_{i,j,k,l}\sum_{\alpha,\beta,\gamma,\delta} \Xi_{ijkl}^{\alpha\beta\gamma\delta} u_i^\alpha u_j^\beta u_k^\gamma u_l^\delta + O(u^5). \quad (10)$$

The extraction of these quartic IFCs ($\Xi_{ijkl}^{\alpha\beta\gamma\delta}$) is extraordinarily demanding computationally because the total number of independent force constant elements scales as $\mathcal{O}(N^4)$, where N denotes the number of atoms in the supercell.

1. Finite-difference approach

The quartic IFCs defined above correspond to the third derivatives of the atomic forces and can be evaluated using a second-order central-difference scheme as

$$\Xi_{ijkl}^{\alpha\beta\gamma\delta} = -\frac{\partial^3 F_i^\alpha}{\partial u_j^\beta \partial u_k^\gamma \partial u_l^\delta} = -\frac{1}{8h^3}\sum_{s_j,s_k,s_l=\pm 1} (s_j s_k s_l) F_i^\alpha\left(s_j h_j^\beta, s_k h_k^\gamma, s_l h_l^\delta\right), \quad (11)$$

where F_i^α represents the force exerted on atom i along the α-direction when a triplet of atoms $m \in \{j, k, l\}$ is simultaneously displaced by a magnitude of $s_m h$ (with $s_m \in \{1, -1\}$) in the β, γ, and δ directions, respectively.

The selection of the displacement magnitude h is critical for ensuring the numerical accuracy of the quartic IFCs. Choosing a value of h that is too small yields an unacceptably low signal-to-noise ratio, where minor force variations are obscured by the numerical noise (such as self-consistent field electronic convergence thresholds) inherent to DFT. Conversely, an excessively large value of h introduces severe discretization errors, as the approximation is bounded by a second-order truncation error, $\mathcal{O}(h^2)$, within the finite-difference formulation.

Noticeably, eight independent force calculations are required to evaluate each irreducible quartic configuration using the central-difference scheme in Eq. (11). By comparison, cubic IFCs evaluated at the same second-order accuracy [$\mathcal{O}(h^2)$] require only four calculations per unique displacement configuration. This doubling of the necessary DFT iterations per configuration, compounding the severe $\mathcal{O}(N^4)$ scaling of the atomic quartets, underscores the massive increase in total computational cost associated with quartic IFC workflows.

Among the specialized toolkits developed for higher-order transport calculations, fourthorder.py[54] is widely utilized to extract quartic IFCs via this finite-difference methodology. While the code implements a default displacement magnitude of $h = 0.01$ Å, the final precision of the computed quartic IFCs remains highly sensitive to this parameter. Rigorous convergence testing with respect to h is, therefore, mandatory to decouple the targeted physical signal from background DFT numerical artifacts without introducing catastrophic truncation errors.

Furthermore, as discussed later (Sec. IV A 1), the optimal value of h is fundamentally non-universal. It depends strongly on the specific material system, the chosen exchange-correlation functional, and the relative stiffness of the constituent interatomic bonds. Consequently, a systematic convergence benchmark must be performed for each distinct computational system to preserve the physical validity of the downstream four-phonon scattering rates.

2. Regression-based Taylor-series fitting

An elegant alternative to the deterministic finite-difference scheme is the regression-based approach, which treats the extraction of IFCs as an optimization problem within a statistical framework. This methodology utilizes a diverse ensemble of disordered atomic configurations and maps the resulting DFT-calculated forces back to the Taylor expansion via a global fitting procedure. In this framework, the potential-energy expansion is reformulated as a linear system of equations. For a given set of arbitrary atomic displacements $\{\boldsymbol{u}\}$ and corresponding quantum-mechanical forces $\{\boldsymbol{F}\}$, the exact relationship is defined by

$$F_i^\alpha = -\frac{\partial U}{\partial u_i^\alpha} = -\sum_j \sum_\beta \Phi_{ij}^{\alpha\beta} u_j^\beta - \frac{1}{2}\sum_{jk}\sum_{\beta\gamma} \Psi_{ijk}^{\alpha\beta\gamma} u_j^\beta u_k^\gamma - \frac{1}{6}\sum_{jkl}\sum_{\beta\gamma\delta} \Xi_{ijkl}^{\alpha\beta\gamma\delta} u_j^\beta u_k^\gamma u_l^\delta. \quad (12)$$

By aggregating structural displacements and corresponding atomic forces across multiple configurations, an overdetermined linear system of equations of the form $\boldsymbol{F} = \mathbf{X}\boldsymbol{\Theta}$ is constructed. Here, $\mathbf{X}$ represents the structural design matrix containing polynomial combinations of displacements, while $\boldsymbol{\Theta}$ denotes the target

23 October 2026 05:10:15

Published under an exclusive license by AIP Publishing

descriptor vector containing the unknown harmonic and anharmonic IFCs (Φ, Ψ, Ξ).

To solve this overdetermined system, two primary regression techniques are widely adopted: Ordinary Least Squares (OLS) and Compressive Sensing Lattice Dynamics (CSLD). The OLS approach minimizes the residual sum of squares between the true DFT forces and the forces predicted by the truncated Taylor expansion model, expressed as

$$\min_{\boldsymbol{\Theta}} \|\boldsymbol{F} - \mathbf{X}\boldsymbol{\Theta}\|_2^2. \tag{13}$$

Conversely, the CSLD paradigm enforces sparsity by introducing an ℓ_1-norm regularization penalty (Lasso regression), which optimizes the following objective function:

$$\min_{\boldsymbol{\Theta}} \frac{1}{2}\|\boldsymbol{F} - \mathbf{X}\boldsymbol{\Theta}\|_2^2 + \lambda\|\boldsymbol{\Theta}\|_1, \tag{14}$$

where λ is a tunable regularization hyperparameter. By incorporating the penalty term $\lambda\|\boldsymbol{\Theta}\|_1$, CSLD effectively screens out negligible or physically redundant interaction channels, retaining only the dominant force constant elements.

Regardless of the choice of optimization algorithm, the predictive accuracy and physical validity of the extracted quartic IFCs remain heavily contingent upon the structural diversity of the training configuration set. Three primary sampling techniques are standard in this regard:

1. **Thermal Snapshots:** Atoms are stochastically displaced according to the harmonic vibrational amplitudes at a target temperature based on the quantum-mechanical Bose–Einstein distribution.[35] This strategy ensures that the potential-energy surface is sampled in regions highly relevant to actual quantum statistical occupancy.
2. ***Ab initio* Molecular Dynamics (AIMD):** Configurations are extracted directly from an AIMD trajectory, mapping out the true phase space explored by the crystal at thermal equilibrium. To guarantee statistical independence and minimize temporal correlation between snapshots, configurations are typically drawn from extensive trajectories spanning 10 000–50 000 timesteps.
3. **Stochastic Displacements:** All atoms within the supercell are simultaneously shifted along random, uncorrelated direction vectors.

Among these approaches, generating thermal snapshots is highly advantageous because it naturally incorporates quantum zero-point fluctuations and provides an effective temperature-dependent renormalization of the force constants. Typically, between 50 and 500 independent supercell configurations are required to construct a sufficiently overdetermined design matrix for robust quartic IFC extraction. Computational toolkits such as temperature dependent effective potential (TDEP),[35] CSLD,[55] and hiPhive[52] serve as the primary open-source software interfaces for performing these force-displacement regression tasks.

D. Step-4: Four-phonon scattering phase space

The next essential component for evaluating higher-order anharmonicity is the four-phonon scattering phase space (P_4). This quantity is obtained by integrating over all kinematically allowed phonon quartets $\{\boldsymbol{q}\nu, \boldsymbol{q}_1\nu_1, \boldsymbol{q}_2\nu_2, \boldsymbol{q}_3\nu_3\}$ and filtering for those specific combinations that satisfy the fundamental selection rules governing crystal momentum and energy conservation,

$$\boldsymbol{q} \pm \boldsymbol{q}_1 \pm \boldsymbol{q}_2 + \boldsymbol{q}_3 = \mathbf{G}, \tag{15}$$

and

$$\omega \pm \omega_1 \pm \omega_2 = \omega_3, \tag{16}$$

where $\mathbf{G}$ denotes a reciprocal lattice vector (with $\mathbf{G} = \mathbf{0}$ for normal processes and $\mathbf{G} \neq \mathbf{0}$ for Umklapp scattering).

Derived solely from the harmonic phonon dispersion relations, the scattering phase space represents the total volume of available scattering channels allowed by the crystal's symmetry and vibrational spectrum, completely decoupled from the actual strength of the scattering potential. Because four-phonon interactions involve an additional degree of freedom within the conservation equations relative to three-phonon processes, P_4 is typically several orders of magnitude larger than its three-phonon counterpart (P_3).

To put this in perspective, for a four-phonon scattering calculation utilizing a $10 \times 10 \times 10$ $\boldsymbol{q}$-point grid within a relatively small five-atom unit cell, a brute-force evaluation of P_4 would require checking approximately 10^{16} modal combinations. Fortunately, by restricting the wavevector $\boldsymbol{q}_1$ to the symmetry-irreducible Brillouin zone and utilizing the crystal momentum conservation rule to implicitly define the final wavevector ($\boldsymbol{q}_3 = \mathbf{G} - \boldsymbol{q}_1 \mp \boldsymbol{q}_2 \mp \boldsymbol{q}_3$), the active computational complexity is reduced to approximately 10^{13}–10^{14} evaluations. In comparison, evaluating the three-phonon phase space P_3 requires only $\sim 10^9$ combinations, highlighting a staggering 10^4–10^5 increase in complexity for fourth-order interactions. Furthermore, storing these scattering matrices in memory to facilitate an efficient iterative solution to the BTE demands roughly 10 GB of RAM for three-phonon processes; for four-phonon scattering, this memory footprint scales upward by several orders of magnitude, posing a formidable data-storage bottleneck.

It is worth noting that because the scattering phase space is a purely harmonic quantity, its numerical evaluation can be carried out independently without requiring the prior calculation or storage of the quartic IFCs.

E. Step-5: Four-phonon thermal conductivity

The final stage of the computational workflow involves substituting the reciprocal-space scattering matrix elements and the phase space summations into the BTE. To manage the extraordinary computational complexity, numerical tools such as the FourPhonon extension to the ShengBTE package have been developed.[54] Given that the $\mathcal{O}(N^4)$ scaling of the four-phonon scattering matrix is inherently parallelizable, a graphics processing unit (GPU)-accelerated version of the FourPhonon package is also available.[56] However, at the time of writing, this GPU-accelerated

23 October 2026 05:10:15

Published under an exclusive license by AIP Publishing

framework supports only the RTA solution of the BTE for higher-order four-phonon scattering calculations.

F. Optional (recommended) steps: Machine-learning acceleration

To circumvent the prohibitive $\mathcal{O}(N^4)$ scaling and the massive displacement-configuration requirements of quartic IFC calculations, machine-learning (ML) approaches have emerged as transformative solutions. By training an ML surrogate model on a sparse, intelligently sampled subset of DFT configurations, the anharmonic potential-energy surface can be mapped with *ab initio* accuracy at a fraction of the traditional computational cost. In our previous work, we demonstrated that the computational cost for anharmonic IFC extraction can be reduced by an order of magnitude while preserving the accuracy of the predicted thermal conductivity to within 10% with this approach.[57] However, within that same investigation, we observed that while this approach remains highly accurate and efficient when coupled with regression-based schemes for IFCs extraction, its accuracy degrades significantly when paired with traditional finite-difference-based methodologies.[57]

Similarly, ML strategies have been reported to significantly accelerate the direct evaluation of phonon–phonon scattering rates.[58–60] Notable methodologies in this regard include (i) the stochastic sampling approach introduced by Guo *et al.*,[58,59] which leverages the fact that because the total scattering rate per phonon mode in Eqs. (4) and (7) is computed via summation over millions of individual scattering events, a maximum likelihood estimation framework[59] can be utilized to infer the true scattering rate by averaging over only a sparse fraction of these events, and (ii) the direct ML-based prediction of phonon lifetimes.[60] In the latter approach, an ML surrogate model is trained using computationally inexpensive phonon observables as descriptors to predict mode-resolved lifetimes. By training the model on a small, representative subset of the phonon Brillouin zone, the scattering rates for the remaining modes can be rapidly predicted across the full zone. Typical fast-to-compute physical descriptors include phonon frequencies, group velocities, participation ratios, and Grüneisen parameters.

Importantly, the above two ML paradigms are complementary; when deployed in tandem, they have been reported to provide a cumulative computational speedup of two orders of magnitude across a diverse dataset of 230 materials.[60]

While the stochastic methodology is integrated into the widely adopted FourPhonon computational package, a critical limitation must be noted: at the time of writing, this stochastic sampling acceleration implementation within the FourPhonon package remains strictly limited to the RTA solution of the BTE.

IV. CASE STUDIES

A. Quartic interatomic force constants

1. Finite-difference step size

As detailed in Sec. III C, the quartic IFCs required for four-phonon scattering calculations can be evaluated via either the finite-difference approach or regression-based Taylor-series fitting. In this section, we evaluate two distinct model systems to systematically demonstrate the influence of numerical noise and displacement step size (h) on the fidelity of the extracted force constants: (i) face-centered cubic argon, modeled using a 12-6 Lennard-Jones potential to represent a prototypical soft material,[61,62] and (ii) silicon, modeled using the Stillinger–Weber empirical potential to represent a prototypical stiff material.[63] These specific systems are chosen because their interatomic interactions are defined analytically by empirical formulations. Consequently, they provide a pristine reference environment where highly accurate baseline IFCs can be evaluated, allowing us to isolate purely numerical and algorithmic artifacts without the compounding electronic noise inherent to DFT calculations.

For each system, we initially compute the reference harmonic, cubic, and quartic IFCs using displacement step sizes of $h = 0.001$, 0.005, and 0.005 Å, respectively. Because these values are extracted from analytical empirical potentials, they are treated as the *exact, pristine* baseline IFCs. To systematically evaluate how numerical instabilities impact the accuracy of the extracted force constants, artificial noise was manually injected into the computed interatomic forces prior to the IFC extraction process. For each force component, one decimal digit was randomly selected from a prescribed set of decimal positions and replaced with a different randomly chosen digit (0–9, excluding the original digit). Four perturbation models were considered by modifying the fifth, sixth, seventh, or eighth decimal places, respectively. The perturbations were applied independently to every force component, without introducing any spatial or directional correlations between different atoms or force components. We evaluated these four distinct noise levels across seven different step sizes ranging from $h = 0.001$–0.05 Å. To ensure statistical significance and establish robust error bounds, for each perturbed configuration, 100 independent trials of numerically perturbed forces were generated at each discrete noise amplitude. The resulting sensitivity of the extracted force constants is presented in Fig. 3, where the standard deviation across the 100 trials is used as a quantitative measure of the numerical error propagated to the final IFCs.

The left and right panels of Fig. 3 display the results for the soft and stiff systems, respectively. Furthermore, to assess how noise sensitivity correlates with the absolute strength of interatomic interactions, the extracted IFCs were sorted in decreasing order of magnitude. The results are explicitly analyzed for two representative cases: (a) the absolute largest IFC (designated as the *large* IFC) and (b) a small IFC valued at approximately 10% of the maximum magnitude (designated as the *small* IFC).

Figure 3 highlights several vital trends regarding the numerical stability of the extracted IFCs. First, the propagated numerical noise in the extracted force constants increases with the order of the IFC expansion; quartic force constants exhibit the highest susceptibility to noise, followed by cubic and harmonic terms, respectively. Second, for a given system configuration, the *small* force constants consistently display a higher relative propagated noise than their *large* counterparts. Third, soft materials systems inherently accumulate substantially more numerical noise within their extracted IFC arrays compared to stiffer systems. Fourth, the resulting noise in the IFCs is highly sensitive to the coupled effects of the force perturbations and the chosen finite-difference step size (h). Specifically, to restrict the numerical error of the extracted

23 October 2026 05:10:15

Published under an exclusive license by AIP Publishing

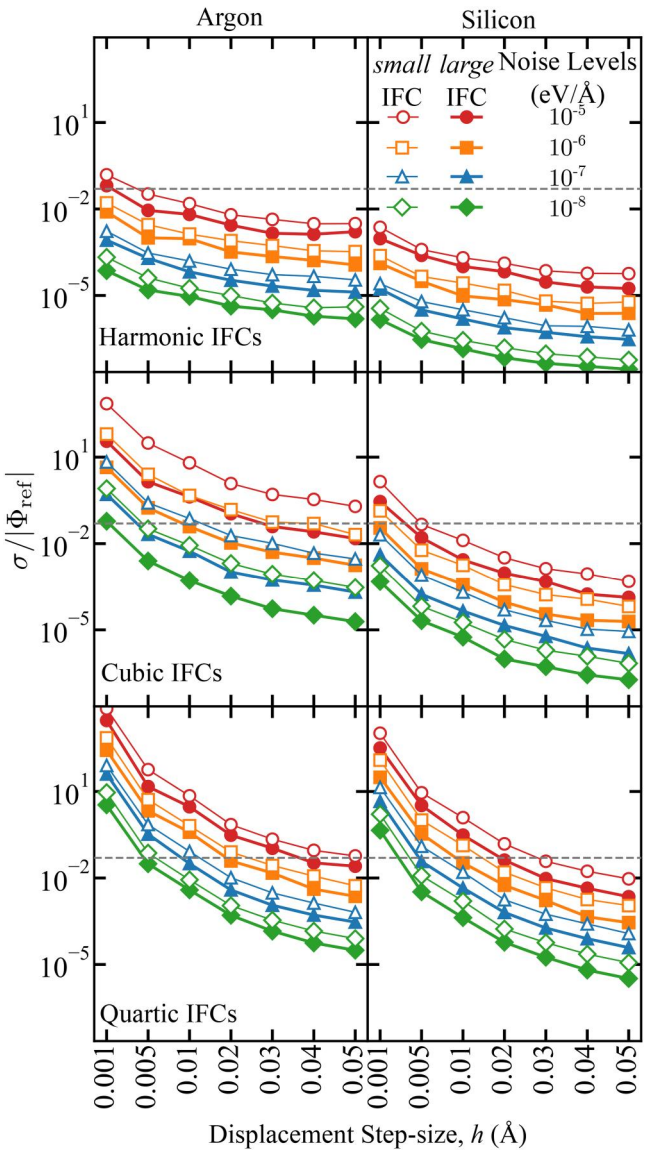


FIG. 3. Impact of numerical force noise on the fidelity of interatomic force constants (IFCs) extracted via the finite-difference method. Each datapoint represents the ratio of the standard deviation (σ) of the IFCs, computed across 100 noisy force datasets, to the reference value of the *pristine* IFCs (Φ_{ref}). The reference harmonic, cubic, and quartic IFCs are evaluated using displacement step sizes of 0.001, 0.005, and 0.005 Å, respectively. The horizontal dashed lines in each panel denote a 5% standard deviation threshold. With a force noise level of 10^{-6} eV/Å, the quartic IFCs require a step size of 0.02 Å or larger.

IFCs to under 5% under a baseline force noise threshold of 10^{-6} eV/Å, for harmonic IFCs, a step size of 0.001 Å or greater is sufficient. For cubic interactions, the baseline step size of 0.005 Å remains sufficient only for the stiff system and is required to be increased to at least 0.03 Å for the soft system. For the quartic terms, a stringent minimum step size of 0.02 and 0.03 Å is required for the stiff and soft systems, respectively, to ensure numerical convergence. Consequently, selecting an appropriate step size for higher-order IFC extraction via the finite-difference approach requires careful, case-by-case convergence testing.

We note that similar behavior was reported by Zhou *et al.*,[64] who highlighted the extreme sensitivity of four-phonon-limited lattice thermal conductivity to the finite-difference displacement step size. They demonstrated that optimal step sizes vary not only across different materials but also between exchange-correlation functionals for a given system, necessitating dedicated convergence tests for each material–functional pair.

2. Regression approach

Next, the numerical error propagation is evaluated for the alternative regression-based framework (Fig. 4) for the soft and stiff model systems. For this, the baseline harmonic IFCs were initially extracted via the finite-difference method using a displacement step size of $h = 0.001$ Å. Subsequently, the harmonic eigenspectrum is computed and is employed to generate an ensemble of 200

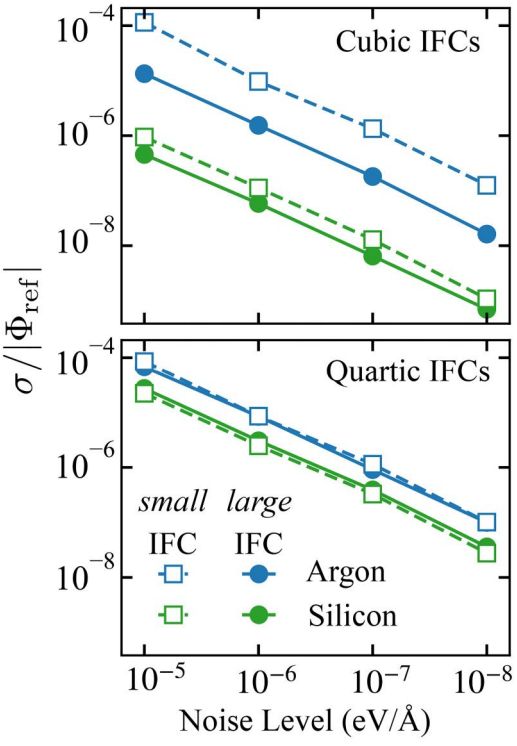


FIG. 4. Impact of numerical force noise on the fidelity of interatomic force constants (IFCs) extracted via the least square regression approach. Each datapoint represents the ratio of the standard deviation (σ) of the IFCs, computed across 100 noisy force datasets, to the reference value of the *pristine* IFCs (Φ_{ref}). The reference cubic and quartic IFCs are evaluated using the finite-difference method with a baseline displacement step size of 0.005 Å. The extracted IFCs are resilient to numerical noise in atomic forces for both systems.

23 October 2026 05:10:15

Published under an exclusive license by AIP Publishing

uncorrelated, thermally perturbed supercell configurations, wherein all atoms were simultaneously displaced from their respective equilibrium positions.[17,35,65] Following the determination of the total calculated forces, the harmonic force contributions were systematically subtracted to isolate the anharmonic residuals. Finally, a simultaneous least squares Taylor-series regression was executed on this dataset to extract the corresponding cubic and quartic IFCs. The resulting regression-fitted cubic and quartic force constants are compared directly against the noise-free baseline values obtained via the finite-difference method (evaluated at a standard step size of $h = 0.005$ Å) for both the *large* and *small* IFC elements across the two material systems (Fig. 4).

Interestingly, the regression-based approach demonstrates remarkable resilience to numerical noise for both model systems. Specifically, the relative percentage deviation from the noise-free finite-difference reference values remains strictly bounded below 0.01% for both the cubic and quartic IFCs. This exceptional fidelity holds true across both the soft and stiff material regimes, spanning both the *large* and *small* IFC elements, thereby highlighting the robust numerical stability of the regression framework for higher-order IFCs extraction.

3. Numerical noise in DFT forces

Considering that the extracted IFCs are highly sensitive to numerical fluctuations in interatomic forces, it is imperative to rigorously assess the intrinsic numerical noise inherent to standard DFT workflows. For this purpose, we selected BAs as a prototypical validation system. Electronic structure calculations are performed using the Vienna *Ab Initio* Simulation Package (VASP) version 6.4.2.[49] The primitive unit cell of BAs was structurally relaxed employing a $10 \times 10 \times 10$ Γ-centered Monkhorst–Pack $\boldsymbol{k}$-point grid, combined with a plane wave kinetic energy cutoff of 415 eV (corresponding to 1.3 times the maximum recommended cutoff value, ENMAX). The self-consistent functional is converged to ensure that the change in total electronic energy is less than 10^{-8} eV.

We constructed a $4 \times 4 \times 4$ supercell from the fully optimized primitive cell and displaced a single atom from its equilibrium position by 0.05 Å. Subsequently, we carried out supercell force calculations utilizing a $4 \times 4 \times 4$ $\boldsymbol{k}$-point mesh of the electronic Brillouin zone, combined with Gaussian electronic smearing using a broadening width of $\sigma = 0.05$ eV. To minimize real-space interpolation errors and maximize numerical precision, the internal VASP flags were configured with projection operators evaluated in reciprocal space (LREAL = .FALSE.), high precision (PREC = Accurate), and the standard electronic optimization algorithm (ALGO = Normal). All calculations were executed within the generalized gradient approximation using the PBEsol exchange-correlation functional[66] and implemented via the projector augmented-wave (PAW) method.[67]

We investigated the sensitivity of the obtained forces on four parameters: (i) an increase in the plane wave kinetic energy cutoff beyond $1.3 \times$ ENMAX, (ii) variations in the electronic wavevector grid, (iii) changes in the electronic minimization algorithm (ALGO), and (iv) adjustments to the parallelization parameters (NPAR/NCORE) to alter the workload distribution across multi-CPU architectures (see Table I).

We find that increasing both the plane wave kinetic energy cutoff (ENCUT) and the electronic wavevector grid density ($\boldsymbol{k}$-point mesh) leads to noticeable variations in the calculated forces. While the forces exhibit non-monotonic convergence with respect to ENCUT, the variations associated with $\boldsymbol{k}$-point mesh density decrease monotonically upon mesh refinement. Given that a supercell size of 128 atoms, a $2 \times 2 \times 2$ $\boldsymbol{k}$-point mesh, and a plane wave energy cutoff of $1.5 \times$ ENMAX represent the standard parameter configurations typically employed for IFC evaluations, the computed atomic forces are converged to an accuracy threshold of approximately 10^{-4} eV/Å under these settings.

We note that although this threshold of 10^{-4} eV/Å remains excessively large for extracting quartic IFCs via the finite-difference approach (Sec. IV A 1), the variations in the plane wave energy cutoff and electronic wavevector grid density could introduce systematic shifts or uniform drifts in the atomic forces,

TABLE I. Restoring force components evaluated on a boron atom displaced by 0.05 Å from its equilibrium position within a 4 × 4 × 4 relaxed supercell of cubic boron arsenide. First-principles calculations are performed via density functional theory as implemented in the Vienna Ab initio Simulation Package.[49] The sensitivity of the atomic forces is benchmarked across various key numerical parameters: plane wave kinetic energy cutoff (ENCUT), electronic wavevector grid sampling (KPOINTS), self-consistent field electronic minimization algorithms (ALGO), and parallel workload distribution strategies (NCORE).

ENCUT	FORCE (eV/Å)	ALGO	FORCE (eV/Å)
$1.30 \times$ ENMAX	−0.832 483 34	Normal	−0.832 483 34
$1.50 \times$ ENMAX	−0.832 433 92	Fast	−0.832 483 04
$1.75 \times$ ENMAX	−0.832 707 04	VeryFast	−0.832 483 24
$2.00 \times$ ENMAX	−0.832 704 22	Conjugate	−0.832 477 36
$2.25 \times$ ENMAX	−0.832 924 88	All	−0.832 478 72
KPOINTS	FORCE (eV/Å)	NCORE	FORCE (eV/Å)
$1 \times 1 \times 1$	−0.840 615 39	1	−0.832 483 07
$2 \times 2 \times 2$	−0.832 006 57	2	−0.832 486 77
$3 \times 3 \times 3$	−0.832 292 07	4	−0.832 488 41
$4 \times 4 \times 4$	−0.832 483 34	8	−0.832 488 41
$5 \times 5 \times 5$	−0.832 550 12	16	−0.832 489 24

23 October 2026 05:10:15

Published under an exclusive license by AIP Publishing

which can still cancel out during the symmetric subtractions inherent to finite-difference schemes.

In contrast, varying the electronic minimization algorithm introduces a force variance of 10^{-5} eV/Å, whereas altering the parallelization mapping yields a variance of 10^{-6} eV/Å. Because the discrepancies arising from the choice of minimization algorithm and parallel task distribution introduce purely stochastic fluctuations rather than systematic physical drifts, these algorithmic and hardware-mapping variations serve as a direct, quantitative measure of the intrinsic numerical noise embedded within first-principles forces. Consequently, these results suggest that the intrinsic numerical noise floor for the calculated forces resides between 10^{-5} and 10^{-6} eV/Å.

It is important to emphasize that, due to the high computational cost of the large number of force evaluations required to extract quartic IFCs via the finite-difference approach, DFT parameters are often reduced to coarser values in the evaluation of quartic IFCs. However, our error-propagation analysis shows that quartic IFCs exhibit the highest relative sensitivity to numerical noise. Consequently, compromising the precision of the underlying DFT parameters is expected to disproportionately amplify errors within the quartic IFCs compared to more resilient harmonic and cubic counterparts.

B. Four-phonon scattering rate

Next, we continue utilizing BAs as our test system to discuss the convergence of various numerical parameters when evaluating higher-order four-phonon scattering processes. We start by considering three-phonon and phonon–isotope scattering mechanisms within the RTA solution of the BTE to obtain convergence for the three-phonon-limited thermal conductivity. For extracting force constants, we employed a $5 \times 5 \times 5$ supercell with Γ-point sampling of the electronic Brillouin zone, 420 eV plane wave energy cutoff, and 0.01 eV Gaussian smearing. Accounting for only three-phonon and phonon–isotope scattering, we obtain a converged (within 1%) thermal conductivity of ∼1450 W/m K at 300 K, utilizing a cubic interaction cutoff of the third nearest neighbor shell and a $16 \times 16 \times 16$ phonon wavevector grid, based on finite-difference-extracted cubic IFCs evaluated at a displacement step size of 0.01 Å.

Given that the converged parameters determined for the three-phonon-limited baseline typically establish an upper numerical bound (with four-phonon properties often converging at comparatively coarser parameter values), we constrain the quartic interaction cutoff to the third nearest-neighbor shell and the phonon wavevector grid to $16 \times 16 \times 16$ while conducting the four-phonon convergence tests.

The convergence of the four-phonon thermal conductivity with respect to the finite-difference displacement step size and the quartic interaction cutoff distance is reported in Table II. These reported results are obtained using the RTA solution of the BTE and include phonon–isotope scattering. Through these convergence tests, the four-phonon-limited thermal conductivity is found to be converged at ∼949 W/m K when employing a finite-difference displacement step size of 0.01 Å in conjunction with a nearest-neighbor (first-neighbor) interaction cutoff shell. Notably, this converged value falls within ∼ 2% of the thermal conductivity obtained via the thermal snapshot approach utilizing the regression-based framework. The latter approach offers a distinct computational advantage, as it completely circumvents the myriad of resource-intensive DFT force evaluations typically required to sweep and validate step-size convergence within conventional finite-difference workflows. We note that, strictly speaking, interatomic force constants derived from thermal snapshot regression sample a temperature-dependent region of the potential energy surface that differs from the 0 K potential surface sampled by the finite-difference approach. For BAs, however, both methods yield consistent thermal conductivity values at 300 K owing to the small mean square thermal displacements of the constituent atoms (<0.01 Å^2) from their equilibrium positions.

TABLE II. Lattice thermal conductivity of cubic boron arsenide at 300 K evaluated using a $10 \times 10 \times 10$ phonon wavevector grid by including three-phonon, four-phonon, and phonon–isotope scatterings. The results are obtained using the relaxation time approximation of the Boltzmann transport equation and are compared across different nearest-neighbor interaction cutoffs, finite-difference displacement step sizes, and thermal snapshot regression frameworks.

	Step size (Å)			
Interaction cutoff (Å)	0.01	0.02	0.03	Regression
2.1	949	954	954	930
3.4	942	955	951	919
4.0	925	970	968	926

It is important to emphasize that the convergence behavior of the finite-difference step size and the quartic interaction cutoffs can be coupled. Specifically, if the magnitude of the numerical noise inherent to the extracted quartic IFCs is comparable to the physical values of the long-range force constants, the lattice thermal conductivity may fail to exhibit a physically meaningful convergence trend. These artifacts arise entirely from the underlying numerical noise floor embedded within the interatomic forces: as the neighbor cutoff distance scales upward, the true physical changes in forces are expected to attenuate rapidly; however, the presence of stochastic noise with a comparable magnitude can artificially register as non-negligible interactions beyond the legitimate physical range, culminating in erratic, unconverged thermal conductivity values.

The convergence of BAs' thermal conductivity with the phonon wavevector grid for the four-phonon scattering processes is reported in Fig. 5. As anticipated, the grid density required to achieve a converged lattice thermal conductivity when accounting for four-phonon processes is considerably lower compared to the three-phonon-only case. Specifically, for BAs, a $10 \times 10 \times 10$ phonon wavevector grid, corresponding to 6000 total phonon modes, is sufficient to achieve numerical convergence. In our experience, typically, three-phonon-limited thermal conductivity necessitates a dense wavevector grid of approximately 30 000–60 000 phonon modes to reach convergence, and the four-phonon-inclusive counterpart reaches convergence with a significantly coarser grid with 5000–20 000 phonon modes.[29]

23 October 2026 05:10:15

Published under an exclusive license by AIP Publishing

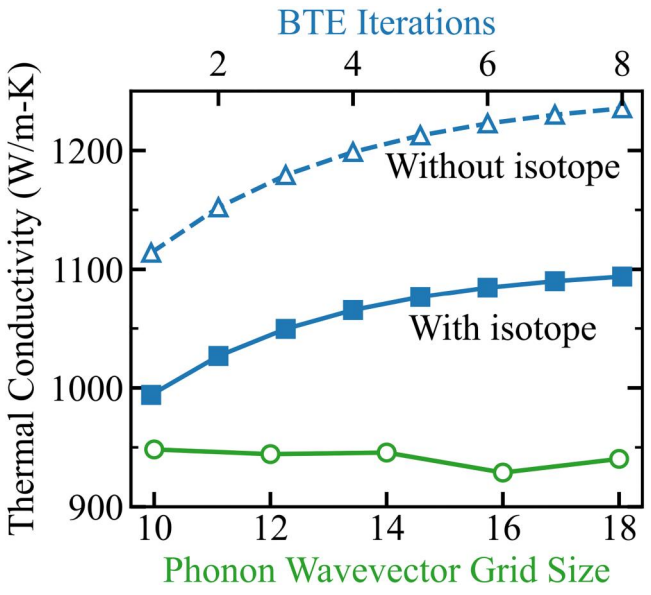


FIG. 5. The convergence of the lattice thermal conductivity of BAs, accounting for three-phonon, four-phonon, and phonon–isotope scattering, as a function of phonon wavevector grid sampling (green, lower axis) and Boltzmann transport equation (BTE) full-solution iteration count (blue, upper axis). The wavevector grid convergence is evaluated within the relaxation time approximation (RTA), whereas the full iterative solution of the BTE is computed using a converged 10 × 10 × 10 grid (converged with RTA solution of the BTE). For completeness, iterative BTE results without phonon–isotope scattering are also included.

After establishing a converged phonon wavevector grid and quartic interaction cutoff within the RTA framework, we finally solve the linearized BTE iteratively (the full solution) to correctly account for the non-resistive, momentum-conserving nature of normal scattering processes (Fig. 5). The resulting fully converged lattice thermal conductivity values, accounting for four-phonon interactions via the iterative solution of the BTE, are ∼1100 W/m K and ∼1235 W/m K at 300 K, with and without the inclusion of phonon–isotope scattering, respectively. These computed values align well with the experimentally measured bounds reported for high-quality bulk crystalline BAs samples, which range from 900 to 1300 W/m K at room temperature.[21,68,69]

C. Computational cost

In Sec. IV B, the convergence of the lattice thermal conductivity was carried out by extending the interaction range up to the third-nearest-neighbor shell. In the limiting case, fully converged results require a truncation radius that extends at least to the second-nearest-neighbor shell. Within the regression-fitting framework, the force evaluations required to extract quartic IFCs are derived from a single set of DFT calculations, amounting to a fixed computational cost of 200 supercell DFT force evaluations in the present study. In stark contrast, when the conventional finite-difference method is employed, the workload scales drastically, requiring 96, 544, and 1536 individual DFT force evaluations for the first-, second-, and third-neighbor shells of the quartic IFCs, respectively. Furthermore, if a systematic convergence check across three distinct displacement step sizes is performed, the computational burden of the finite-difference approach is multiplied by an additional factor of 3. Consequently, the total number of DFT evaluations required to establish convergence via the regression approach remains strictly bounded at approximately 200 configurations, representing a massive computational reduction compared to the more than 1600 (bare minimum with second neighbor shell) evaluations demanded by the finite-difference approach.

Furthermore, the magnitude of the restoring forces generated for individual atoms subjected to small, isolated perturbations in the finite-difference approach is often comparable to the intrinsic prediction errors of ML force fields. Therefore, the direct applicability of ML models to finite-difference-based IFC extraction is severely limited.[57] Conversely, in the regression framework, since all the atoms in the supercell are simultaneously displaced, either randomly or according to a representative thermal population, the resulting restoring forces are significantly larger than the baseline ML errors. Consequently, when coupled with the regression approach, the computational cost associated with IFCs extraction can be drastically reduced via ML acceleration. For the BAs test system, we demonstrate that training a simple Smooth Overlap of Atomic Positions-Gaussian Approximation Potential (SOAP-GAP) model[70,71] on only ten perturbed configurations is sufficient. The forces for the remaining configurations can then be accurately predicted using the trained ML model. Remarkably, the lattice thermal conductivity obtained using the IFCs extracted from this ten-structure-trained ML surrogate is 904 W/m K, demonstrating exceptional agreement with the 910 W/m K obtained when utilizing the full dataset of 200 direct DFT supercell evaluations and a 16 × 16 × 16 phonon wavevector grid (Fig. 6).

As discussed in Sec. III D, another severe computational bottleneck in evaluating four-phonon-limited lattice thermal conductivity arises from the explicit calculation of the four-phonon scattering rates themselves. Achieving numerical convergence for the thermal conductivity typically requires sampling up to 20 000 phonon modes; for instance, the 16 × 16 × 16 wavevector grid utilized here for BAs corresponds to 24 576 total phonon modes. For the considered BAs system, evaluating the raw four-phonon scattering rates requires ∼340 cpu-hours on the 16 × 16 × 16 grid for the RTA solution of the BTE. In comparison, the three-phonon scattering calculations executed on the identical wavevector grid require only ∼15 cpu-hours.[72] The substantially high computational requirement of higher-order four-phonon scattering evaluations can be effectively bypassed through ML-based acceleration strategies. By implementing the stochastic sampling methodology of Guo *et al.*[58,59] and accounting for only 1% of the total scattering events to determine the four-phonon lifetimes, the obtained thermal conductivity is 910 W/m K, which demonstrates exceptional agreement with the value obtained without any ML acceleration (Fig. 6). By leveraging this ML approach, a computational speedup of more than 10 × is achieved. However, care must be exercised to ensure the numerical convergence of the ML-driven results (e.g., by systematically varying the fraction of accounted scattering processes from 1% to 5%) while remaining cognizant of

23 October 2026 05:10:15

Published under an exclusive license by AIP Publishing

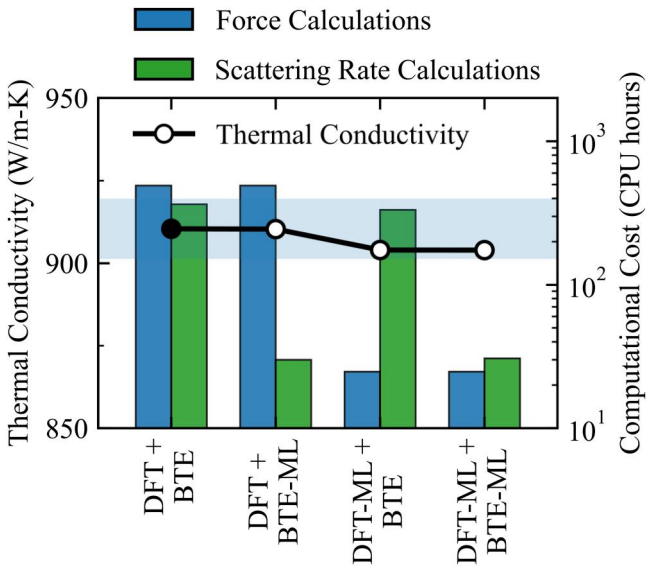


FIG. 6. Comparison of computed lattice thermal conductivity for cubic boron arsenide alongside the corresponding computational cost across different frameworks. All underlying first-principles force evaluations are performed using a $5 \times 5 \times 5$ supercell with electronic Γ-point sampling. The regression approach used in the above calculations employs quartic interaction cutoffs extending to the first nearest-neighbor shell, evaluated using $16 \times 16 \times 16$ phonon wavevector grids, within the relaxation time approximation. The shaded gray region designates a $\pm 1\%$ error bound centered around the baseline DFT+BTE solution (black-filled circle).

the intrinsic limitations of the underlying computational implementation (such as its restriction to the RTA solution in the FourPhonon package implementation at the time of writing).[59]

V. COMPUTATIONAL PACKAGES

Table III summarizes the computational packages for lattice dynamics and phonon thermal transport calculations. These software packages use different methods for calculating harmonic, cubic, and quartic interatomic IFCs, as well as for implementing the BTE solver. The diversity of available approaches, including finite-difference, least squares fitting, direct, iterative, and variational methods, enables the investigation of thermal transport properties across a variety of material systems.

VI. OUTLOOK

With the increasing availability of high-performance computational resources and open-source software packages, the inclusion of higher-order four-phonon scattering processes has become routine in BTE-based evaluations of lattice thermal conductivity. This paradigm shift has enabled a more comprehensive description of the underlying phonon transport physics, consistently yielding closer quantitative agreement with experimental measurements. The consideration of four-phonon scattering processes is particularly vital for high-temperature applications and for materials exhibiting either anomalously low or exceptionally high thermal conductivities. However, given that these higher-order computational methodologies are still in their relative infancy and the field is actively working to fully understand their nuances,

23 October 2026 05:10:15

TABLE III. Features and computational capabilities of open-source software packages for evaluating interatomic force constants (IFCs) and solving the phonon Boltzmann transport equation (BTE).

	Interatomic force constant			Lattice thermal conductivity	
Package	Harmonic	Cubic	Quartic	κ_l (3ph)	κ_l (3ph+4ph)
Phonopy[48]	Finite-difference	…	…	…	…
Phono3py[48]	Finite-difference		…	RTA, direct	…
almaBTE[73]	…	…	…	RTA, iterative, direct, variance-reduced Monte Carlo	…
ALAMODE[74]	Least square fitting		Elastic net, adaptive lasso	RTA, iterative	…
Phoebe[75]	…	…	…	RTA, iterative, variational, direct	…
TDEP[76]	Least square fitting			RTA, iterative	RTA, Iterative
hiphive[52]	Multiple regression algorithms			…	…
CSLD[55]	ℓ_1-norm lasso regression			…	…
kALDo[77]	Finite-difference			RTA, iterative, Quasi-harmonic Green-Kubo	…
FOCEX[78]	Finite-difference			…	…
THERMACOND[79]	…	…	…	RTA, iterative, direct	…
Thirdorder.py[51]	…	Finite-difference	…	…	…
ShengBTE[51]	…	…	…	RTA, iterative	…
Fourthorder.py[54]	…	…	Finite-difference	…	…
FourPhonon[54]	…	…	…	…	RTA, iterative
GPU_PBTE[80]	…	…	…	RTA, iterative	RTA, iterative

Published under an exclusive license by AIP Publishing

special care must be exercised when executing and interpreting four-phonon-based calculations.

From a computational standpoint, it is imperative to rigorously establish the convergence of lattice thermal conductivity with respect to all key numerical parameters. While several studies in the literature bypass these systematic convergence tests by citing the prohibitive computational expense of higher-order interactions, the heightened sensitivity of four-phonon processes to numerical settings makes such verification even more critical before drawing definitive physical conclusions. As demonstrated herein for BAs, integrating ML frameworks effectively mitigates this computational burden, reducing the computational overhead of four-phonon scattering evaluations to a level comparable to that of standard three-phonon calculations.

Furthermore, convergence behavior remains exceptionally sensitive to the specific material system and the underlying simulation cell configuration. For instance, the thermal conductivity of BAs evaluated using an $5\times5\times5$ supercell with Γ-only sampling of the Brillouin zone yields fully converged quartic IFCs at a finite-difference displacement step size of 0.01 Å; however, convergence is notably lost with this step size when IFCs are extracted utilizing a $4\times4\times4$ supercell with a $4\times4\times4$ Brillouin zone sampling mesh in the study of Zhou *et al.*[64] Nonetheless, the converged thermal conductivity obtained here with the iterative solution of the BTE with isotope scattering compares well with that reported in Ref. 64 (∼1100 W/m K in the present study compared to 1171 W/m K in Ref. 64).

While the test cases presented here (Sec. IV A 1) establish a reliable baseline step size for extracting quartic force constants via the finite-difference approach, the convergence of the phonon thermal conductivity may still be achieved at smaller step sizes due to multiple factors, including the cancellation of errors during the thermal conductivity calculation.

For investigations reporting on multiple material systems or executing high-throughput screening, it is vital to establish independent convergence criteria across multiple, if not all, target systems rather than extrapolating from a single, idealized prototype. Furthermore, when extraordinary or counterintuitive physics are reported, such as an order-of-magnitude reduction in lattice thermal conductivity upon the inclusion of four-phonon processes, or drastically contrasting roles of fourth-order scattering across different phases of a two-dimensional material, it is paramount that special care be taken to isolate and understand the physical origin of the observed phenomena.

Finally, we emphasize that four-phonon scattering alone does not capture the complete spectrum of phonon thermal transport physics, particularly in extremely anharmonic, low-thermal-conductivity materials. In such highly anharmonic regimes, other higher-order effects, such as the temperature renormalization of interatomic IFCs and phonon frequencies, lattice thermal expansion, and multi-channel thermal transport (cohesive wave-like and particle-like behaviors), often play a more dominant role than four-phonon scattering itself.[29,33]

VII. CONCLUSIONS

In this tutorial, we have presented a comprehensive computational guide for evaluating lattice thermal conductivity with inclusion of higher-order four-phonon scattering processes. We established the physical and structural criteria that necessitate fourth-order anharmonic treatments in crystalline solids, followed by a detailed, hierarchical breakdown of the numerical workflow designed to enable researchers to implement and optimize their own computational pipelines.

Through systematic sensitivity analyses of model systems with analytical force fields, we demonstrated the critical impact of numerical noise and the displacement step size on the fidelity of the extracted interatomic force constants (IFCs) using the finite-difference approach. We showed that quartic IFCs are inherently more sensitive to force perturbations than lower-order IFCs, with soft materials experiencing higher noise propagation due to their characteristically flatter potential-energy surfaces. The regression-based Taylor-series IFC fitting approach demonstrates exceptional resilience to these numerical fluctuations.

To bridge these findings with first-principles workflows, the intrinsic numerical noise floor of density functional theory (DFT) force calculations was systematically quantified within the VASP framework using cubic boron arsenide (BAs) as a representative material. By isolating stochastic variations arising from numerical electronic minimization algorithms (ALGO) and hardware parallelization (NPAR/NCORE) from systematic shifts driven by the plane wave kinetic energy cutoff (ENMAX) and ***k***-point grid density, we established that the intrinsic DFT force noise floor resides between 10^{-5} and 10^{-6} eV/Å.

Moving to parameter convergence, we demonstrated that the regression-based IFC extraction techniques offer a distinct computational advantage over finite-difference methods by eliminating the need for exhaustive step-size convergence. Furthermore, we explored machine-learning acceleration strategies for both IFC extraction and four-phonon scattering rate evaluation. We showed that these strategies provide more than an order-of-magnitude reduction in computational time for four-phonon-limited thermal-conductivity calculations without sacrificing predictive accuracy.

Looking to the future of thermal-conductivity prediction, the systematic benchmarks established in this work provide a rigorous foundation for extending to even more complex transport regimes. While the integration of four-phonon scattering represents a major milestone, critical advances continue to be made by coupling these higher-order interactions with finite-temperature frequency shifts (renormalization), complex structural defect scattering, and phonon–electron interactions.

ACKNOWLEDGMENTS

The authors acknowledge the financial support from the Advanced Research Grant, Anusandhan National Research Foundation, India (Grant No. ANRF/ARG/2025/000326/PS). The calculations were carried out on the Praganak supercomputing facility of IIT Bombay and Param Rudra (located at IIT Bombay, India) supercomputing facility provided by the Centre for Development of Advanced Computing (CDAC).

AUTHOR DECLARATIONS

Conflict of Interest

The authors have no conflicts to disclose.

23 October 2026 05:10:15

Published under an exclusive license by AIP Publishing

Author Contributions

Ankit Jain: Conceptualization (equal); Formal analysis (equal); Funding acquisition (equal); Investigation (equal); Methodology (equal); Project administration (equal); Resources (equal); Software (equal); Supervision (equal); Writing – original draft (lead); Writing – review & editing (equal). **Rajan Kumar:** Data curation (equal); Formal analysis (equal); Validation (equal); Visualization (equal); Writing – review & editing (equal). **Jyotishraj Thoudam:** Data curation (equal); Formal analysis (equal); Investigation (equal); Validation (equal); Visualization (equal); Writing – review & editing (equal). **Nidheesh Virakante:** Data curation (equal); Formal analysis (equal); Investigation (equal); Validation (equal); Visualization (equal); Writing – review & editing (equal).

DATA AVAILABILITY

The data that support the findings of this study are available from the corresponding author upon reasonable request.

REFERENCES

[1]D. G. Cahill, W. K. Ford, K. E. Goodson, G. D. Mahan, A. Majumdar, H. J. Maris, R. Merlin, and S. R. Phillpot, J. Appl. Phys. **93**, 793 (2003).
[2]G. Slack, J. Phys. Chem. Solids **34**, 321 (1973).
[3]D. A. Broido, A. Ward, and N. Mingo, Phys. Rev. B **72**, 014308 (2005).
[4]K. Esfarjani and H. T. Stokes, Phys. Rev. B **77**, 144112 (2008).
[5]K. Esfarjani, G. Chen, and H. T. Stokes, Phys. Rev. B **84**, 085204 (2011).
[6]L. Lindsay, Nanoscale Microscale Thermophys. Eng. **20**, 67 (2016).
[7]A. J. McGaughey, A. Jain, H. Y. Kim, and B. Fu, J. Appl. Phys. **125**, 11101 (2019).
[8]L. Lindsay, D. Broido, and N. Mingo, Phys. Rev. B **83**, 235428 (2011).
[9]L. Lindsay, D. Broido, and T. Reinecke, Phys. Rev. B **87**, 165201 (2013).
[10]A. Jain and A. J. McGaughey, Comput. Mater. Sci. **110**, 115 (2015).
[11]A. Jain and A. J. McGaughey, Sci. Rep. **5**, 8501 (2015).
[12]A. Jain, Phys. Rev. B **109**, 155413 (2024).
[13]C. Kittel, *Introduction to Solid State Physics*, 6th ed. (John Wiley & Sons, Inc., New York, 1986).
[14]M. T. Dove, *Introduction to Lattice Dynamics* (Cambridge, Cambridge, 1993).
[15]G. P. Srivastava, *The Physics of Phonons* (CRC Press, 2022).
[16]J. A. Reissland, *The Physics of Phonons* (John Wiley and Sons Ltd., 1973).
[17]A. Jain, Y. Srivastava, A. G. Gokhale, N. Virakante, and H. L. Kagdada, J. Indian Inst. Sci. **105**, 413–436 (2025).
[18]L. Lindsay, D. Broido, and T. Reinecke, Phys. Rev. Lett. **111**, 025901 (2013).
[19]D. Broido, L. Lindsay, and T. Reinecke, Phys. Rev. B **88**, 214303 (2013).
[20]T. Feng, L. Lindsay, and X. Ruan, Phys. Rev. B **96**, 161201 (2017).
[21]J. S. Kang, M. Li, H. Wu, H. Nguyen, and Y. Hu, Science **361**, 575 (2018).
[22]X. Yang, T. Feng, J. Li, and X. Ruan, Phys. Rev. B **100**, 245203 (2019).
[23]T. Feng, and X. Ruan, in *Nanoscale Energy Transport: Emerging Phenomena, Methods and Applications*, edited by B. Liao (IOP Publishing, Bristol, 2020), pp. 2–1–2–44.
[24]Y. Xia, Appl. Phys. Lett. **113**, 073901 (2018).
[25]T. Feng and X. Ruan, Phys. Rev. B **93**, 045202 (2016).
[26]N. K. Ravichandran and D. Broido, Phys. Rev. B **98**, 085205 (2018).
[27]M. Simoncelli, N. Marzari, and F. Mauri, Nat. Phys. **15**, 809 (2019).
[28]J. M. Ziman, *Electrons and Phonons* (Oxford University Press, Clarendon, Oxford, 1960).
[29]A. Jain, Phys. Rev. B **102**, 201201 (2020).
[30]M. Omini and A. Sparavigna, Phys. Rev. B **53**, 9064 (1996).
[31]S.-I. Tamura, Phys. Rev. B **27**, 858 (1983).
[32]A. Jain and A. J. McGaughey, Phys. Rev. B **93**, 081206 (2016).
[33]Y. Xia, K. Pal, J. He, V. Ozoliņš, and C. Wolverton, Phys. Rev. Lett. **124**, 065901 (2020).
[34]T. Feng and X. Ruan, Phys. Rev. B **97**, 045202 (2018).
[35]O. Hellman, P. Steneteg, I. A. Abrikosov, and S. I. Simak, Phys. Rev. B **87**, 104111 (2013).
[36]P. Yadav and A. Jain, Appl. Phys. Lett. **125**, 042110 (2024).
[37]For $CuInTe_2$, the phonon frequency renormalization, lattice thermal expansion corrections are also included.
[38]B. Abeles, D. Beers, G. D. Cody, and J. Dismukes, Phys. Rev. **125**, 44 (1962).
[39]C. J. Glassbrenner and G. A. Slack, Phys. Rev. **134**, A1058 (1964).
[40]J. Yao, N. J. Takas, M. L. Schliefert, D. S. Paprocki, P. E. Blanchard, H. Gou, A. Mar, C. L. Exstrom, S. A. Darveau, P. F. Poudeu *et al.*, Phys. Rev. B **84**, 075203 (2011).
[41]G. Zhou and D. Wang, Phys. Chem. Chem. Phys. **18**, 5925 (2016).
[42]A. Kundu, X. Yang, J. Ma, T. Feng, J. Carrete, X. Ruan, G. K. Madsen, and W. Li, Phys. Rev. Lett. **126**, 115901 (2021).
[43]S. Li, C. Su, Z. Qin, A. Alatas, M. Kunz, T. Yamada, S. D. Kelly, M. H. Upton, A. Gironda, J. Zhao *et al.*, Science **391**, 707 (2026).
[44]L. Lindsay, D. A. Broido, and N. Mingo, Phys. Rev. B **82**, 115427 (2010).
[45]L. Lindsay and D. Broido, Phys. Rev. B **84**, 155421 (2011).
[46]Z. Han and X. Ruan, Phys. Rev. B **108**, L121412 (2023).
[47]L. Lindsay, D. A. Broido, and T. L. Reinecke, Phys. Rev. Lett. **109**, 095901 (2012).
[48]A. Togo, J. Phys. Soc. Jpn. **92**, 012001 (2023).
[49]J. Hafner, J. Comput. Chem. **29**, 2044 (2008).
[50]P. Giannozzi, S. Baroni, N. Bonini, M. Calandra, R. Car, C. Cavazzoni, D. Ceresoli, G. L. Chiarotti, M. Cococcioni, I. Dabo *et al.*, J. Phys.: Condens. Matter **21**, 395502 (2009).
[51]W. Li, J. Carrete, N. A. Katcho, and N. Mingo, Comput. Phys. Commun. **185**, 1747 (2014).
[52]F. Eriksson, E. Fransson, and P. Erhart, Adv. Theory Simul. **2**, 1800184 (2019).
[53]A. J. H. McGaughey, L. Lindsay, H. Bao, T. Hamakawa, R. Juneja, S. Li, W. Li, R. Masuki, F. Meng, H. Meng, T. Pandey, C. Shao, J. Shiomi, T. Tadano, A. Togo, A. Wang, and X. Zhang, J. Appl. Phys. **138**, 135108 (2025).
[54]Z. Han, X. Yang, W. Li, T. Feng, and X. Ruan, Comput. Phys. Commun. **270**, 108179 (2022).
[55]F. Zhou, W. Nielson, Y. Xia, and V. Ozoliņš, Phys. Rev. B **100**, 184308 (2019).
[56]Z. Guo, X. Ruan, and G. Lin, arXiv:2510.00518 (2025).
[57]Y. Srivastava and A. Jain, Phys. Rev. B **110**, 165202 (2024).
[58]Z. Guo, P. Roy Chowdhury, Z. Han, Y. Sun, D. Feng, G. Lin, and X. Ruan, npj Comput. Mater. **9**, 95 (2023).
[59]Z. Guo, Z. Han, D. Feng, G. Lin, and X. Ruan, npj Comput. Mater. **10**, 31 (2024).
[60]Y. Srivastava and A. Jain, Mater. Today Phys. **41**, 101345 (2024).
[61]J. E. Jones, Proc. R. Soc. Lond., Ser. A **106**, 463 (1924).
[62]J. O. Hirschfelder, C. F. Curtiss, and R. B. Bird, *The Molecular Theory of Gases and Liquids* (John Wiley & Sons, 1964).
[63]F. H. Stillinger and T. A. Weber, Phys. Rev. B **31**, 5262 (1985).
[64]H. Zhou, S. Zhou, Z. Hua, K. Bawane, and T. Feng, Appl. Phys. Lett. **123**, 192201 (2023).
[65]D. West and S. Estreicher, Phys. Rev. Lett. **96**, 115504 (2006).
[66]J. P. Perdew, A. Ruzsinszky, G. I. Csonka, O. A. Vydrov, G. E. Scuseria, L. A. Constantin, X. Zhou, and K. Burke, Phys. Rev. Lett. **100**, 136406 (2008).
[67]G. Kresse and D. Joubert, Phys. Rev. B **59**, 1758 (1999).
[68]S. Li, Q. Zheng, Y. Lv, X. Liu, X. Wang, P. Y. Huang, D. G. Cahill, and B. Lv, Science **361**, 579 (2018).
[69]F. Tian, B. Song, X. Chen, N. K. Ravichandran, Y. Lv, K. Chen, S. Sullivan, J. Kim, Y. Zhou, T.-H. Liu *et al.*, Science **361**, 582 (2018).
[70]A. P. Bartók, M. C. Payne, R. Kondor, and G. Csányi, Phys. Rev. Lett. **104**, 136403 (2010).
[71]A. P. Bartók, R. Kondor, and G. Csányi, Phys. Rev. B **87**, 184115 (2013).

23 October 2026 05:10:15

Published under an exclusive license by AIP Publishing

[72]All calculations are performed on compute nodes equipped with 2x Intel Xeon Platinum 8480 processors with 112 cores per node, operating at a base frequency of 2.0 GHz. The nodes are configured with 512 GB DDR5 memory running at 4800 MHz.
[73]J. Carrete, B. Vermeersch, A. Katre, A. van Roekeghem, T. Wang, G. K. Madsen, and N. Mingo, Comput. Phys. Commun. **220**, 351 (2017).
[74]T. Tadano, Y. Gohda, and S. Tsuneyuki, J. Phys.: Condens. Matter **26**, 225402 (2014).
[75]A. Cepellotti, J. Coulter, A. Johansson, N. S. Fedorova, and B. Kozinsky, J. Phys. Mater. **5**, 035003 (2022).
[76]F. Knoop, N. Shulumba, A. Castellano, J. P. Alvarinhas Batista, R. Farris, M. J. Verstraete, M. Heine, D. Broido, D. S. Kim, J. Klarbring *et al.*, J. Open Source Software **9**, 6150 (2024).
[77]G. Barbalinardo, Z. Chen, N. W. Lundgren, and D. Donadio, J. Appl. Phys. **128**, 135104 (2020).
[78]K. Esfarjani, H. Stokes, S. N. Sadeghi, Y. Liang, B. Timalsina, H. Meng, J. Shiomi, B. Liao, and R. Sun, Comput. Phys. Commun. **312**, 109575 (2025).
[79]S. Nayeb Sadeghi, S. Lee, and K. Esfarjani, npj Comput. Mater. **11**, 303 (2025).
[80]B. Zhang, Z. Fan, C. Zhao, and X. Gu, J. Phys.: Condens. Matter **33**, 495901 (2021).

23 October 2026 05:10:15

Published under an exclusive license by AIP Publishing